



Development of nickel supported La and Ce-natural illite clay for autothermal dry reforming of methane: Toward a better resistance to deactivation



Mohcin Akri ^{a,b}, Stéphane Pronier ^a, Tarik Chafik ^b, Ouafae Achak ^b, Pascal Granger ^{c,*}, Pardis Simon ^c, Martine Trentesaux ^c, Catherine Batiot-Dupeyrat ^{a,*}

^a Institut de Chimie des Milieux et Matériaux de Poitiers (IC2MP), Ecole Nationale Supérieure d'Ingénieurs de Poitiers (ENSIP), Université de Poitiers—UMR CNRS 7285, 1 rue Marcel Doré, TSA 41105, 86073 Poitiers cedex 9, France

^b Laboratory LGCVR UAE/L01FST, Faculty of Sciences and Techniques of Tangier, University Abdelmalek Essaadi, Tangier, Morocco

^c Unité de Catalyse et de Chimie du solide (UCCS), Université de Lille 1- UMR CNRS 8181, Cité scientifique Bat C3, 59655 Villeneuve d'Ascq, France

ARTICLE INFO

Article history:

Received 10 October 2016

Received in revised form

15 December 2016

Accepted 20 December 2016

Available online 21 December 2016

Keywords:

Autothermal reforming

Illite clay

Cerium

Lanthanum

Nickel

ABSTRACT

The autothermal dry reforming of methane was performed using natural illite clay as catalyst support. Nickel containing Ce or La promoted catalysts were characterized by XRD and XPS analysis before reaction, after the reduction step and also after 24 h of reaction. The highest catalytic stability was obtained on the La-based catalyst. This result was attributed to the formation of a britholite phase during the reaction resulting from the migration of lanthanum into the bulk. This particular phase could prevent the formation of the FeNi_3 alloy mainly observed on Ce-based material which is presumably much less active than metallic Ni particles towards the dry reforming reaction. A deep surface reconstruction, evidenced by XPS, proceeds during the reaction which complement structural characterization showing significant surface changes in Ni species that cooperate with the basic sites leading to higher catalytic activity and stability.

© 2016 Elsevier B.V. All rights reserved.

1. Introduction

The reforming of methane is an important process to produce syngas with a low H_2/CO ratio suitable for methanol and Fischer-Tropsch synthesis. From an environmental point of view, the reaction converts two low-value greenhouse gases into a major feedstock [1,2].

Noble metals are catalytically very active for the reaction [3–5] but group 8–10 metals such as Fe, Co and Ni are preferentially developed due to their inherent availability and low cost compared to noble metals [6–8]. However, a serious problem is the catalyst deactivation by carbon deposition, especially for Ni catalysts [9]. Therefore, the development of catalysts with weak or no deactivation is of great importance for further industrial applications.

Support effects have been widely investigated and several studies have shown that a high dispersion of the metal species at the support surface can limit the coke deposition [1]. As reported, clas-

sical alumina support alone does not allow to maintain a high catalytic activity, Chen et al. [10] showed that CeO_2 -doped $\text{Ni}/\text{Al}_2\text{O}_3$ catalyst was obviously more stable than the non-promoted alumina support due to the oxygen storage capacity of CeO_2 [11,12]. Verykios et al. [13] found that the use of La_2O_3 improved the catalysts stability through the formation of oxy-carbonate species ($\text{La}_2\text{O}_2\text{CO}_3$) able to gasify the formed carbon deposits.

Clay materials are also interesting as catalyst support due to their low cost, specific properties and structures [14,15]. Debek et al. [16] showed that synthetic clays like hydrotalcites promoted with cerium are relatively active and stable at low temperature (550°C), while Daza et al. [17] managed to improve the catalytic performance and stability at 700°C by doping Ni-Mg-Al mixed oxide with [Ce(EDTA)]. Lanthanum was also used as promoter of Ni hydrotalcite catalysts for the dry reforming of methane. Serrano-Lotina et al. [18] investigated the influence of calcination temperature of La-NiMgAl catalysts derived from hydrotalcite-like structure. The presence of lanthanum in NiMgAl mixed-oxide catalysts improved markedly the catalytic activity in the temperature range of 600 – 700°C , because the introduction of lanthanum increases the total amount of basic sites and the surface Ni content, highlighting the formation of the $\text{La}_2\text{O}_2\text{CO}_3$ phase [19]. Liu

* Corresponding authors.

E-mail addresses: pascal.granger@univ-lille1.fr (P. Granger), catherine.batiot.dupeyrat@univ-poitiers.fr (C. Batiot-Dupeyrat).

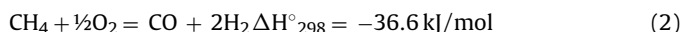
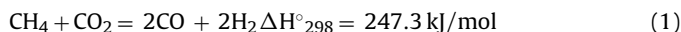
et al. [20] investigated the influence of La-promotion on physico-chemical properties of hydrotalcite catalysts. So far, the authors evidenced bulk NiO segregation and enhanced Ni-reducibility in the presence of lanthanum. Hence, the catalytic activity was higher for the promoted catalyst than for the non-promoted one, while the dry reforming reaction was performed at relatively low temperature: 550 °C.

The use of natural mineral clays as catalytic support was also reported, the superficial chemical properties can be modulated through modification of the inter-laminar space. Of interest, the higher thermal stability to the clay material avoiding its collapse during the calcination step reported by Daza et al. [21]. For example, the incorporation of alumina species, into the inter-laminar spaces of smectite, improves the thermal stability of the material avoiding its collapse during the calcination step.

Thus, illite is one of the most abundant phases of natural clays contained in sedimentary rocks, resulting from the transformation of smectite during diagenesis and metamorphism [22]. Illite is a interlayer-deficient dioctahedral minerals of the mica group with general formula: (K,Ca,Mg) (Al,Mg,Fe)₂(Si,Al)₄O₁₀[(OH)₂,(H₂O)] [23].

In our previous study, we highlighted promising potential of illite containing natural clay as catalyst support for autothermal reforming reaction of methane [24]. The addition of cerium was found to increase significantly the specific surface area of the catalyst and the dispersion of nickel particles on the illite surface. The best performances were obtained with the catalyst containing 15 wt.% Ce, even though the slight deactivation observed 4 h reaction at 800 °C.

It is known that the autothermal reforming process involves the combination of dry reforming (Eq. (1)) and partial oxidation of methane (Eq. (2)) respectively a highly endothermic and mildly exothermic reaction.



The coupling between the two reactions is considered to be more efficient in terms of energy savings as compared to dry reforming alone. Moreover the presence of O₂ in the reaction's stream helps to limit the carbon deposition considered as the major drawback for dry reforming reaction [25].

The aim of the present study was to investigate the catalytic performances of cerium and lanthanum doped illite-based catalysts using nickel as active species. To the best of our knowledge, such comparison has never been reported before. This issue will be addressed by assessing catalytic activity (stability) and the physico-chemical properties of the prepared catalysts. Those ones were comprehensively characterized at different steps: prior to the reaction, after the reduction step and after 24 h of reaction at 800 °C. For this purposes, X-ray diffraction, H₂-TPR, BET surface area, TEM-EDX and X-ray photoelectron spectroscopy were used to examine the catalytic modifications at different stage of reaction on stream.

2. Experimental

2.1. Catalysts preparation

The starting material was a natural clay from the area of Tangier at the north of Morocco. Illite was separated from the raw clay by wet sedimentation according to the Stokes law to allow removal of heavier particles such as quartz. The raw clay was dispersed in deionized water (10% by weight) and submitted to vigorous stirring during four hours until a complete homogenization of the suspension was obtained. After decantation during 24 h, the suspension was recovered and dried at 100 °C then calcined at 500 °C in air dur-

ing 4 h. The targeted catalyst formulations were prepared according to a co-impregnation method of the clay surface by adding the appropriate amount of nitrate precursor of nickel, cerium or lanthanum corresponding to 10 wt.% of Ni and 15 wt.% of Ce or La. The resulting samples were dried at 120 °C during 24 h then calcined in air at 500 °C during 4 h. For the sake of simplicity, they were labeled respectively 10Ni15Ce and 10Ni15La.

2.2. Catalysts characterization

The composition of catalysts was determined by Atomic Emission Spectroscopy with Induced Coupled Plasma (ICP-AES/Optima 200 DV, Perkin Elmer instrument).

Structural properties were characterized by powder X-ray diffraction using a BRUKER AXS D5005 diffractometer with CuK_{α1} = 1,5406 and CuK_{α2} = 1.5439 Å, operated at 40 kV and 40 mA. The diffraction patterns were recorded in the 2θ range 3–80° with a step size of 0.01° and 1 s per step. Phase identification was performed by comparison with the information of the JCPDS database.

Transmission electron microscopy (TEM) measurements were carried out on a JEOL 2100 electron microscope operating at 200 kV, with a LaB₆ filament and equipped with a Gatan ultra scan camera. Microanalysis of Ni, Fe and Ce was carried out by Energy Dispersive X-ray spectroscopy (EDX) in the nanoprobe mode. The mean particle diameter *d* was calculated from the following Equation $d = \sum n_i d_i^3 / \sum n_i d_i^2$. At least 10 images were examined while more than 300 particles were counted and the results were normalized to 100%.

H₂-Temperature-Programmed-Reaction (H₂-TPR) experiments were carried out with a Micromeritics Autochem 2910 equipment using about 160 mg of catalyst. A 5 vol.% H₂/Ar flow of 50 mL min⁻¹ was passed over the catalyst while the temperature was raised at 5 °C/min from ambient to 700 °C and maintained at this temperature for 2 h. The amount of hydrogen consumed was measured with a thermal conductivity detector. Specific Surface areas were measured according to BET procedure. Prior to nitrogen physisorption, samples were out gassed for 30 min at 350 °C. Adsorption – desorption isotherms of nitrogen were determined at –196 °C using 30 vol.% N₂/He as the adsorbate on a Micromeritics Flowsorb II 2300 apparatus.

CO₂-Temperature programmed desorption (CO₂-TPD) was performed using the same apparatus (Micromeritics Flowsorb II 2300). The catalysts were reduced at 600 °C for 90 min using 20%H₂/He (100 mL/min) at a heating rate of 10 °C/min, then purged for 30 min under He. After reduction, the sample was cooled down, CO₂ (5%CO₂/He) was adsorbed at 50 °C for 30 min and weakly adsorbed CO₂ was removed by purging with He during 30 min. The samples were heated from 50 to 800 °C at a heating rate of 10 °C/min in He flow and the desorbed CO₂ was detected by a thermal conductivity detector (TCD).

XPS characterization was carried out with a Kratos AXIS Ultra DLD instrument using a monochromatic Al K_α X-ray source (12 mA, 15 kV). C 1s, O 1s, Ni 2p, Ce 3d and La 3d high resolution spectra were obtained using a 40 eV pass energy. The residual pressure in the analysis chamber was below 9×10^{-10} mbar during analysis. All spectra have been charge corrected to give the Ce4f⁰ peak for stoichiometric CeO₂ at 916.7 eV for cerium oxides based compounds and corrected to give the adventitious C 1s spectral component a binding energy (BE) of 284.8 eV for lanthanum oxides based compounds. Spectra were analyzed using Casa XPS software [26]. Quantification was performed based on the Ni 2p and Ce 3d or La 3d peaks area after a Shirley background subtraction for Ni 2p and La 3d spectra and a linear background subtraction for Ce 3d spectra.

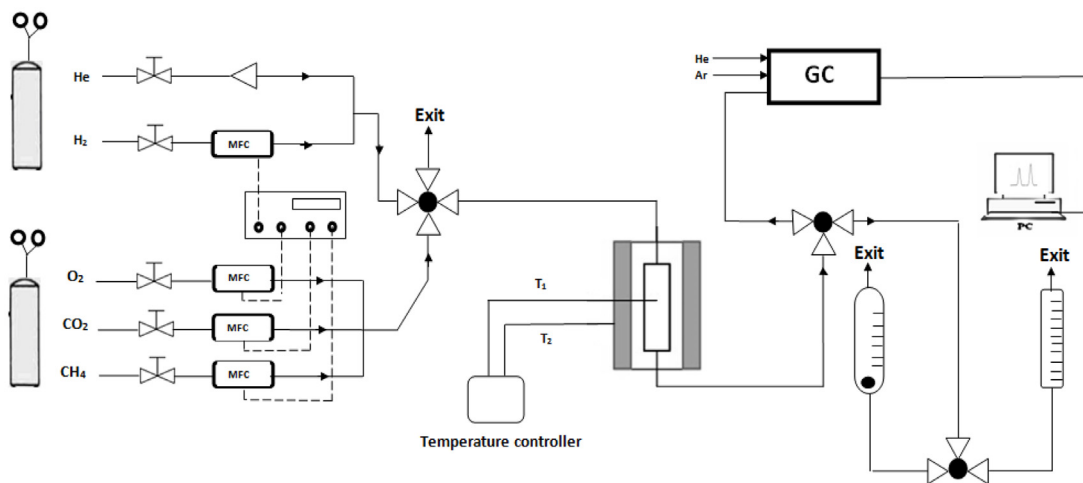


Fig. 1. Experimental setup for catalytic measurements.

2.3. Catalytic tests

The catalysts performances were evaluated at atmospheric pressure in a fixed bed continuous flow quartz reactor (i.d. = 10 mm) containing 100 mg of catalyst sample (see Fig. 1). The catalyst was first reduced in-situ under 20%H₂/He flow at a flow rate of 100 mL/min, at 600 °C during 90 min. The sample was then purged under helium during 30 min at 600 °C and heated at 800 °C at a heating ramp of 10 °C min⁻¹. The reactant mixture (CH₄/CO₂/O₂ = 50/40/10 mL/min) corresponding to a Gas Hourly Space Velocity (GHSV) of 6.0×10^4 mL g⁻¹ h⁻¹ was introduced at 800 °C and kept during the desired reaction time. The temperature was measured with a thermocouple located inside the reactor but without direct contact with the catalyst bed. The reaction products were analyzed using a micro-GC (VARIAN CP4900) equipped with a Poraplot Q (10 m, 0.15 mm), a CP-Sil 5 CB (8 m, 0.15 mm), and a molecular sieve 5 A (10 m, 0.32 mm) columns with TCD detectors to analyze on-line the different gases (H₂, CO, CO₂, CH₄) within 3 min.

3. Results and discussions

3.1. Physicochemical characterization of freshly-prepared catalysts

The illite material used as catalyst support in this study contains mainly SiO₂ (54.4 wt.%) and Al₂O₃ (26.6 wt.%) but also a significant amount of iron oxide (7.6 wt.%) [24], similar to the composition reported by Gailhanou et al. for a typical illite clay [27]. In this study the amount of nickel, lanthanum and cerium was kept unchanged respectively at 10, 15 and 15 wt.% respectively. The composition of the samples obtained after addition of nickel and La or Ce, measured by ICP was closed to the targeted values as shown in Table 1.

The specific surface area value measured on calcined 10Ni and 10Ni15La samples are comparable of respectively 19 and 15 m² g⁻¹.

Table 1
Chemical composition of the catalysts 10Ni, 10Ni15Ce and 10Ni15La (wt.%).

designation	Ni (wt.%)		Ce or La (wt.%)	
	T ^a	M ^b	T ^a	M ^b
10Ni	10	10.2	0	–
10Ni15Ce	10	10.2	15	13.4
10Ni15La	10	9.9	15	14.6

^a T: Target value.

^b M: measured value.

Table 2
BET surface area (m²/g) and porous volume (cm³/g) of 10Ni, 10Ni15Ce and 10Ni15La.

Sample	Surface area (m ² /g)			Vp ^a (cm ³ /g)
	Calc. ^a	Red. ^b	Reac. ^c	
10Ni	19	9	5	0.036
10Ni15Ce	25	15	6	0.064
10Ni15La	15	2	<1	0.040

^a Calcined at 500 °C.

^b After reduction at 600 °C under H₂.

^c After 4 h of reaction.

On the other hand, cerium incorporation leads to the development of porosity as shown in Table 2. These results can be correlated with the differences observed in the N₂ physisorption isotherms obtained with non-promoted, La and Ce-promoted illite (Fig. 2). Thus the isotherms seem to be likely of type-I for illite clay and La-based, whereas Ce-based catalyst shows hysteresis loop of type IV isotherm. The BJH pore size distribution indicates the formation of mesopores with an average size of 15.2 nm for the catalyst 10Ni15Ce.

Fig. 3 shows the XRD patterns of the 10Ni catalyst without promoter. The typical reflections of illite structure with an interlayer space d₀₀₁ = 1 nm at 2θ = 8.8° [28] is clearly visible after calcination. For 10Ni15Ce (Fig. 4a), Broad peaks of NiO (JCPDS n° 01-078-0423) and of CeO₂ (fluorite-type structure) are also observed and the presence of quartz is detected (JCPDS n° 5-490). The presence of lanthanum oxide (JCPDS n° 98-064-1602) and NiO on 10Ni10La is also detected after calcination (see Fig. 5a).

The reducibility of illite and the two catalysts 10Ni15Ce and 10Ni15La was studied by H₂-TPR experiments (Fig. 6). Three main reduction processes are observed for the both catalysts, the reduction peaks being shifted to lower temperatures with cerium as compared to lanthanum. The lowest temperature H₂-consumption process corresponds to the reduction of NiO into metallic nickel. The two contributions at around 500 and 750 °C correspond to the reduction of the illite support as shown in Fig. 6, and more precisely to oxidic Fe₂O₃ species in octahedral sites of the clay [29]. The existence of Ce³⁺/Ce⁴⁺ redox pairs can explain the promoting effect of Ce, which enable the electron transfer favoring the reduction of NiO and Fe₂O₃ species in the neighboring sites [17].

For both catalysts, a complete reduction of NiO proceeds at temperature lower than 600 °C. Consequently, according to the TPR profile, the catalysts were reduced in-situ prior to the reaction at 600 °C.

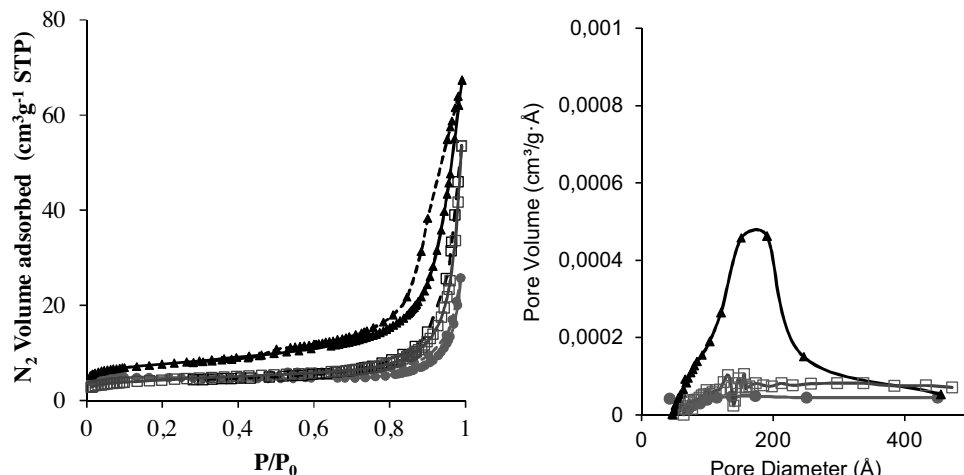


Fig. 2. N_2 adsorption-desorption isotherms and pore size distribution obtained from the adsorption loop for illite, 10Ni15Ce and 10Ni15La.
●: illite, □: 10Ni15La, ▲: 10Ni15Ce.

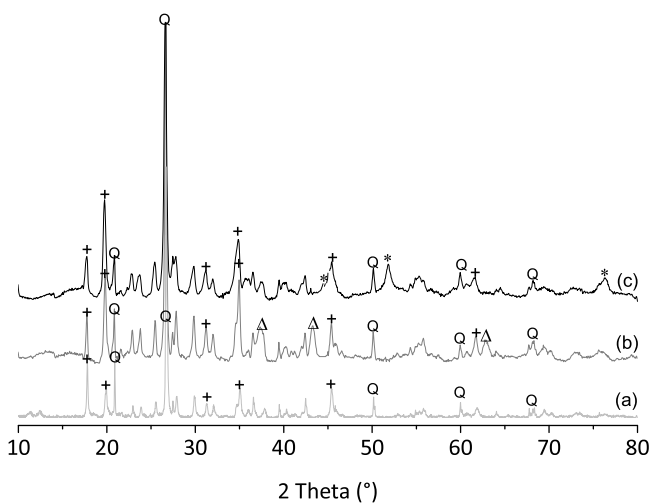


Fig. 3. XRD patterns of illite after calcination a), 10Ni/illite after calcination b), 10Ni/illite after reduction c).

+ Illite, Q quartz, Δ NiO , * Ni .

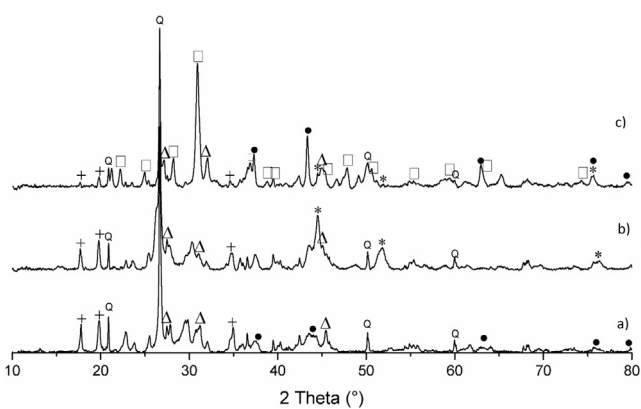


Fig. 5. XRD patterns of 10Ni15La after calcination a), after reduction at 600°C b) and after 24 h of reaction c).

+ Illite, Q quartz, Δ La_2O_3 (98-064-1602), ● NiO , \square $\text{La}_{0.31}\text{O}_{26}\text{Si}_{6.24}$ (britholite 98-016-1478).

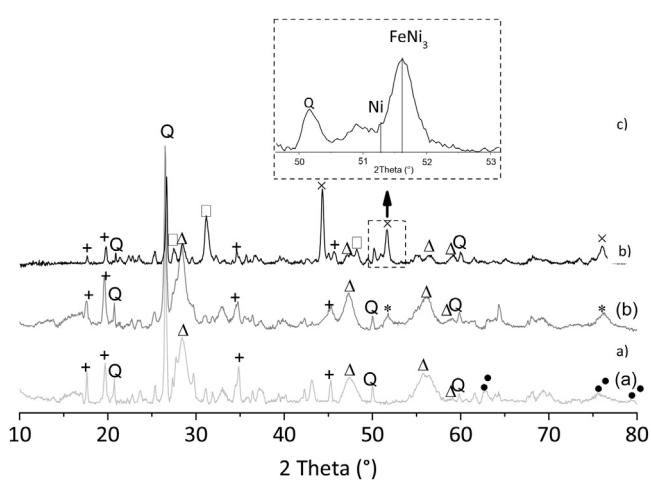


Fig. 4. XRD patterns of 10Ni15Ce after calcination a), after reduction at 600°C b) and after 24 h of reaction c).

+ Illite, Q quartz, Δ CeO_2 (98-015-5613), \times FeNi_3 (awaruite 98-004-0334), ● NiO , * Ni , \square $\text{Ce}_{4.67}\text{O}_{13}\text{Si}_3$ (98-000-9378).

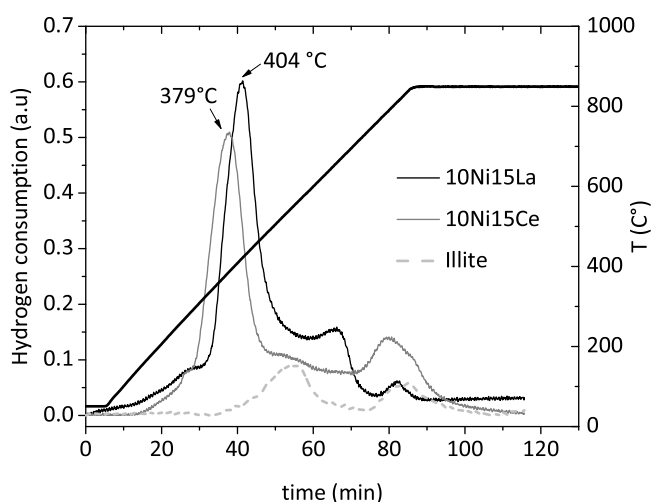


Fig. 6. H_2 -TPR experiments on, illite, calcined 10Ni15Ce and 10Ni15La ($5\%H_2/Ar$ flow of 50 mL min^{-1} at 5°C min^{-1} from room T to 700°C).

Table 3

Hydrogen consumption by H₂-TPR (5%H₂/Ar flow of 50 mL min⁻¹ at 5 °C min⁻¹ from room T to 700 °C) and percentage of NiO reduced for 10Ni, 10Ni15Ce and 10Ni15La.

Catalyst	H ₂ consumption for NiO reduction (mL STP/g) (±2%)		NiO Reductibility (%)
	Estimated ^a	Determined ^b	
10Ni	39.1	37.2	95
10Ni15Ce	39.0	39.5	100
10Ni15La	37.8	35.3	93

^a Estimated: calculated from the nominal composition of the material according to the following reaction: NiO + H₂ = Ni + H₂O.

^b Determined: obtained from H₂-TPR by decomposition of the peaks using the mathematical software Origin.

The hydrogen consumption values were calculated from the integrated peak area using the mathematical software Origin. H₂ uptakes are collected in Table 3. The theoretical amount of hydrogen consumed was determined by the volume of hydrogen required to reduce NiO into Ni⁰⁰, based on the elemental composition. The results show that the volume of hydrogen consumed corresponds to the targeted values within the experimental error (estimated at ±5%).

XRD patterns recorded on reduced samples are reported in Figs. 3 c), 4 b) and 5 b). The presence of reduced Ni⁰ is evidenced by reflections at 2θ = 44.5 and 54° for the three catalysts 10Ni, 10Ni15Ce and 10Ni15La. Note that no significant bulk detectable modification of the illite support was observed by XRD after the reduction step. On the other hand, the pre-reductive thermal treatment has a significant detrimental effect on the specific surface area (see Table 2).

After the reduction step, TEM analysis clearly shows the presence of spherical particles of nickel (Fig. 7). The mean nickel particle size distribution are respectively equal to 34.2, 16.3 and 14.3 nm for respectively 10Ni, 10Ni15Ce and 10Ni15La, proving that the addition of cerium or lanthanum stabilize smaller metallic Ni particles at the surface of the illite support despite the lower specific surface areas on reduced samples especially on 10Ni15La. The beneficial effect of cerium for stabilizing the nickel dispersion was already pointed out by Li et al. [30]. Martinez et al. [31] also reported that lanthanum allows to obtain small nickel particles after reduction treatment.

The CO₂ TPD profiles of 10Ni15Ce and 10Ni15La are reported in Fig. 8. As expected three main peaks are observed in a temperature range of 100–800 °C. The first peak at 100–150 °C, representative of weak bronsted basic sites, presents a low intensity for the Ce and La promoted catalysts. The shape of the second peak between 350 and 580 °C, corresponding to medium-strength Lewis acid-base sites, of both catalysts is very similar. The third mean peak is larger and shifted to higher temperature for La-promoted catalyst compared to Ce-based catalyst, pointing to stronger basic sites as a consequence of the presence of lanthanum.

The total amount of desorbed CO₂ was estimated from the integration of CO₂-TPD peak area: 100 and 120 μmol/g of CO₂ was respectively desorbed from 10Ni15Ce and 10Ni15La highlighting the presence of different basic sites that could be involved in the overall catalytic process.

3.2. Catalysts activity and stability

The catalysts were first reduced in flowing hydrogen (20% vol. in He) at 600 °C for one hour, the catalytic reaction was carried out using a mixture of methane, carbon dioxide and oxygen with the following composition: CH₄/CO₂/O₂ = 50/40/10 mL/min. The oxygen concentration was chosen according to optimum value earlier reported by Amin and Yaw [32]. The reaction was performed at 800 °C using a low contact time (GHSV = 60,000 mL h⁻¹ g⁻¹). First, the catalytic tests were carried out with the illite support alone

after reduction under 20%H₂/He at 600 °C. Methane and carbon dioxide conversion was respectively equal to 11 and 4%, this activity could be attributed to the metallic iron sites present in the clay substrate. The reaction with the nickel supported catalyst was performed during 24 h, as shown in Fig. 9 and reported in a previous investigation [24], the CH₄ and CO₂ conversions measured for 10Ni15Ce catalyst decrease regularly with time on stream. The addition of lanthanum on illite, drastically improves the catalytic stability: methane and carbon dioxide conversion are maintained at 80% and 63% respectively after 24 h of reaction. Similar results were observed by Serrano et al. [18] using Ni-Mg/hydrotalcite catalysts promoted with lanthanum. The authors attributed the high stability to the favorable CO₂ adsorption at the surface of the basic sites of lanthanum oxide. Da costa et al. [20] showed also a very good stability of La-promoted Ni-hydrotalcite-derived catalysts, which was attributed to the gasification of amorphous carbon deposits, resulting in lower overall carbon deposition, but the reaction was performed at relatively low temperature: 550 °C against 800 °C in our study. The lower CO₂ conversion compared to CH₄ conversion and the H₂/CO ratio slightly lower than unity, suggests the involvement of complex chemistry at the surface of 10Ni15La and 10Ni15Ce with various competitive reactions i.e. dry reforming of methane partial oxidation of methane, methane combustion, Reverse-Water-Gas-Shift, methanation reactions... The carbon balance closed to 100% and stable during 24 h of reaction, strongly suggests that carbon deposition is not favoured for the two catalysts and underlines the beneficial effect of oxygen. The reaction was further carried out with 10Ni15La catalyst during 72 h of reaction. As shown in Fig. 10 the catalyst exhibits stable performances during 40 h of reaction and then methane and carbon dioxide conversion slightly decrease with time on stream. However the carbon balance is maintained closed to 100% during 60 h of reaction, proving that carbon deposition is not favoured under the experimental conditions used in this study. After 60 h of reaction the decrease of CH₄ conversion associated with the increase of H₂/CO ratio suggest that methane cracking occurs.

The thermogravimetric curves obtained after 24 h of reaction (Fig. 11) are very similar for the two catalysts: a low weight loss is observed at low temperature, representing only 0.2 and 0.4% in weight for respectively 10Ni15Ce and 10Ni15La. From a temperature of about 350 °C, a weight gain is observed, it can compensate the weight loss associated to carbon removal, consequently the exact amount of carbon deposition could not easily determined. The high carbon balance proves however that the amount of carbon deposition is low for the two catalysts.

3.3. Physicochemical characterization of spent catalyst after autothermal dry reforming reaction and reaction mechanism

In order to explain the observed catalytic behavior in terms of stability, the catalysts were characterized straightforwardly after reaction by *ex situ* S_{BET}, XRD, TEM and XPS.

3.3.1. S_{BET}, XRD and TEM analysis

The specific surface area of the catalysts decrease significantly after the reduction step at 600 °C and after four hours of reaction at 800 °C (Table 2). The reconstruction of the material under the reactants and products mixture at high temperature: 800 °C can explain the very low surface area of materials particularly for lanthanum based catalyst.

The diffraction patterns recorded on 10Ni15Ce catalyst after 24 h of reaction evidence the presence of a Ni-Fe alloy with the composition: FeNi₃ (JCPDS n°98-004-0334). Additional reflections appear ascribed to Ce_{4.67}O₁₃Si₃ (JCPDS n°98-000-9378) whereas those characteristic of ceria strongly attenuates suggesting an extensive formation of Ce_{4.67}O₁₃Si₃ at the expense of CeO_x (Fig. 4c). Note that

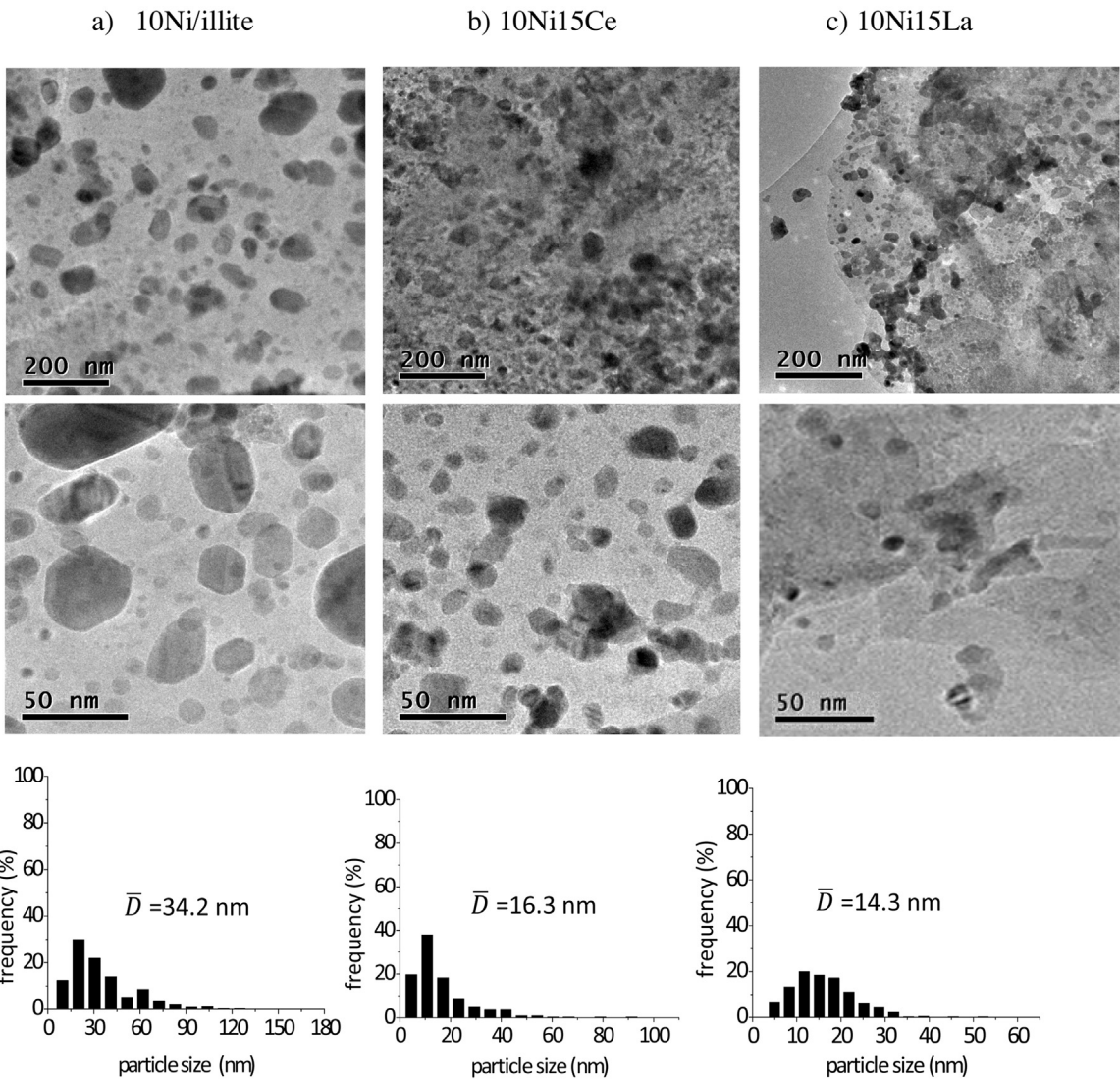
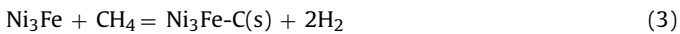


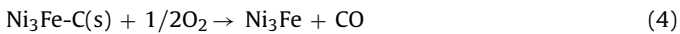
Fig. 7. TEM analysis after reduction of 10Ni, 10Ni15Ce and 10Ni15La.

the alloy and the mixed oxide $\text{Ce}_{4.67}\text{O}_{13}\text{Si}_3$ are only observed after reaction while their presence was not detected after the reduction step. The formation of such alloy is corroborated by TEM analysis (Fig. 12) while EDX analysis confirmed the simultaneous presence of nickel and iron. Note that carbon fibers are also observable, proving that carbon deposition proceeds during time on stream in some extent. The stabilization of Ce(III) species in $\text{Ce}_{4.67}\text{O}_{13}\text{Si}_3$ agrees with a more extensive reduction under reaction conditions at much higher temperature than those encountered during the reductive pre-activation treatment.

The FeNi_3 alloy is less active than dispersed Ni° particles [29], it is also suspected to be involved in carbon deposition according to the following equation (Eq. (8)) proposed by Galvita et al. [33]:



However the presence of oxygen in the feed gases can help carbon removal according to the reaction:



Note that carbon balance remains high even if the catalytic activity decreases sharply with time on stream (Fig. 9).

Furthermore cerium is known as an interesting promoter that easily gasifies carbon deposition due to its redox properties

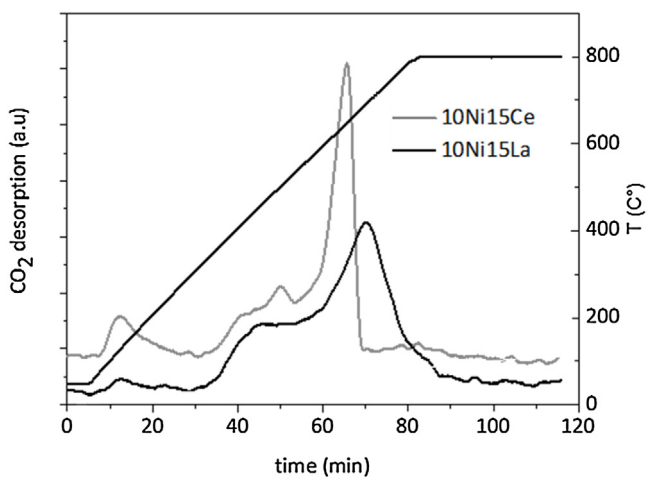


Fig. 8. CO₂-TPD for 10Ni15La and 10Ni15Ce.

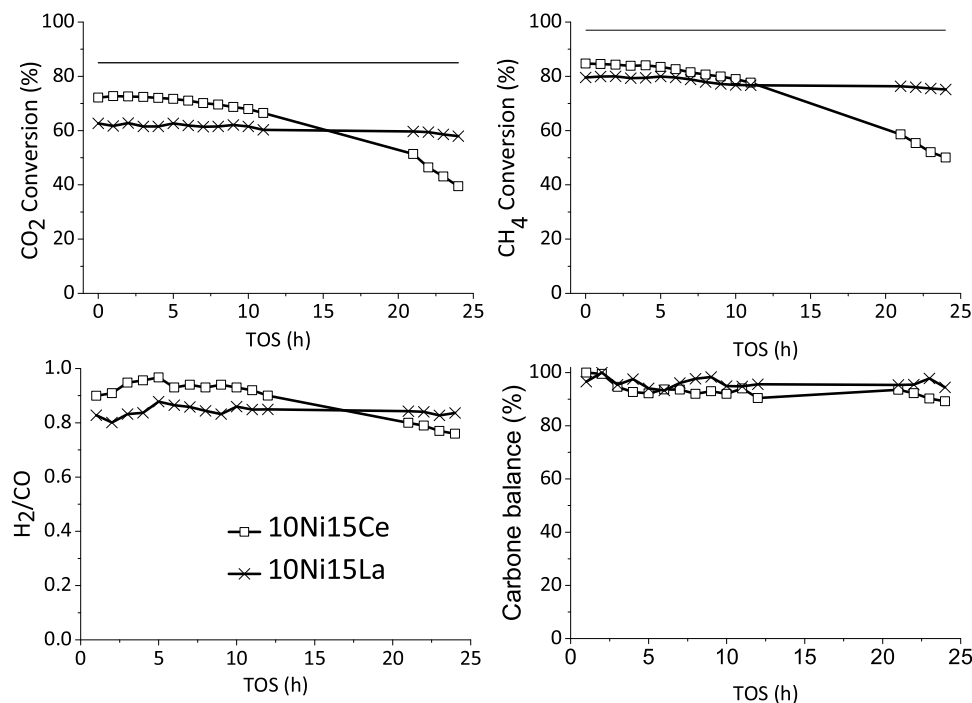


Fig. 9. Catalytic activity and stability of 10Ni15Ce and 10Ni15La, T = 800 °C, CH₄/CO₂/O₂ = 50/40/10, GHSV = 60,000 mL h⁻¹ g⁻¹.

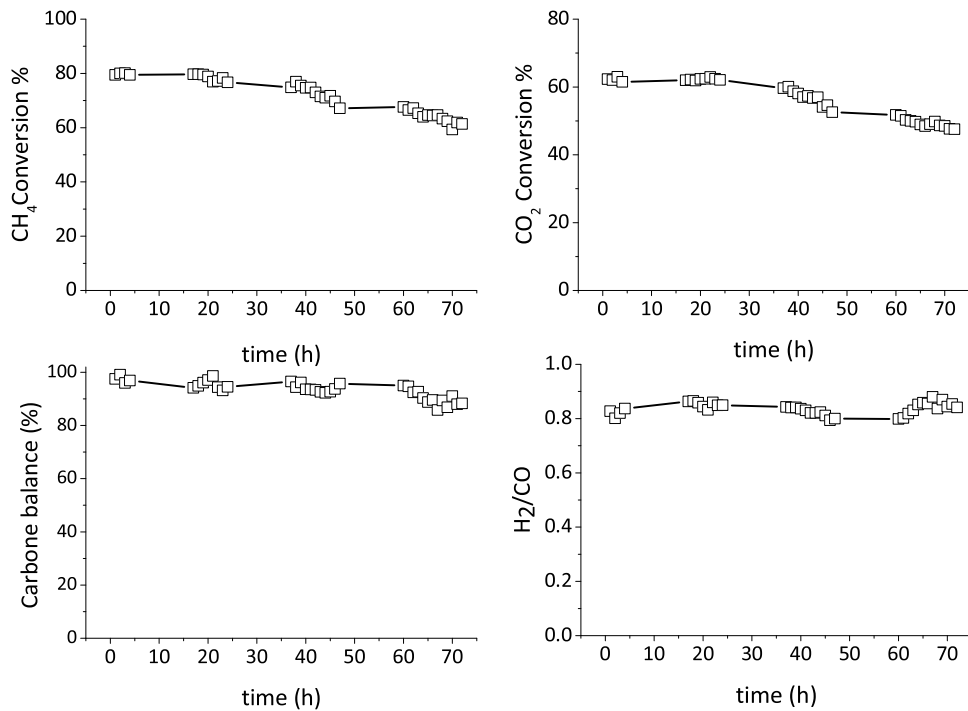
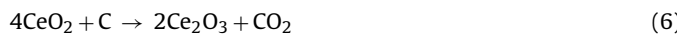


Fig. 10. Long term experiment for 10Ni15La, T = 800 °C, CH₄/CO₂/O₂ = 50/40/10, GHSV = 60,000 mL h⁻¹ g⁻¹.

(Ce⁴⁺/Ce³⁺) [34]. The presence of oxygen vacancies facilitates CO₂ adsorption/dissociation and gasification of the CH_x species according to Eqs. (5) and (6) [35]:



The oxygen introduced in the reactant flow can adsorb at the surface defects of ceria due to the presence of oxygen vacan-

cies. The resulting chemisorbed oxygen species can be evolved as lattice oxygen restoring the reduction of Ce⁴⁺ according to: 2 Ce³⁺ + ½ O₂ → 2Ce⁴⁺ + O²⁻. Consequently, part of the chemisorbed oxygen reacts at the surface of Ce-based catalyst instead of participating to carbon removal. Let us notice that the formation of Ce_{4.67}O₁₃Si₃ could have detrimental effects on the oxygen storage properties weakening the valency changes which originate such properties.

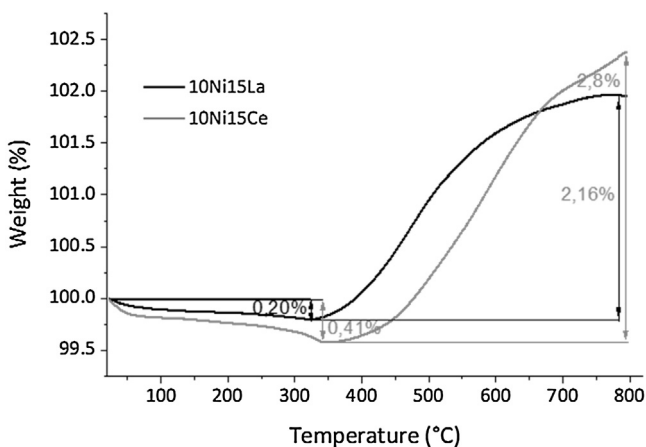


Fig. 11. TGA analysis after 24 h of reaction over 10Ni15Ce and 10Ni15La.

Over the La-promoted illite support, the Ni₃Fe alloy is not detected after reaction but interestingly the presence of mixture of NiO and britholite phase (JCPDS n°98-016-1478) besides Ni⁰ is clearly evidenced by XRD (Fig. 5). The reflections ascribe to La_{9.31}O₂₆Si_{6.24} becomes predominant on the used catalyst but those corresponding to La₂O₃ still remains clearly distinguishable which could suggest that bulk transformations in the course of the reaction occur in lower extent than those related to the formation of Ce_{4.67}O₁₃Si₃. The formation of NiO species after 6 h of reaction, at 850 °C over NiCe-x/SiO₂ under a flow of CH₄/CO₂/O₂: 40/20/10 mL/min, was also reported by Li et al. [30] proving that the presence of oxygen in the gaseous phase is able to oxidize the reduced nickel species at high temperature. TEM and EDX analysis (Fig. 13) confirm that the nickel-iron alloy is not favorably formed during reaction over La-based illite catalyst. The diffusion of lanthanum into the clay structure can be proposed according to EDX analysis. It is thus possible to propose that, the migration of lanthanum into the bulk illite structure can prevent the formation of Ni₃Fe.

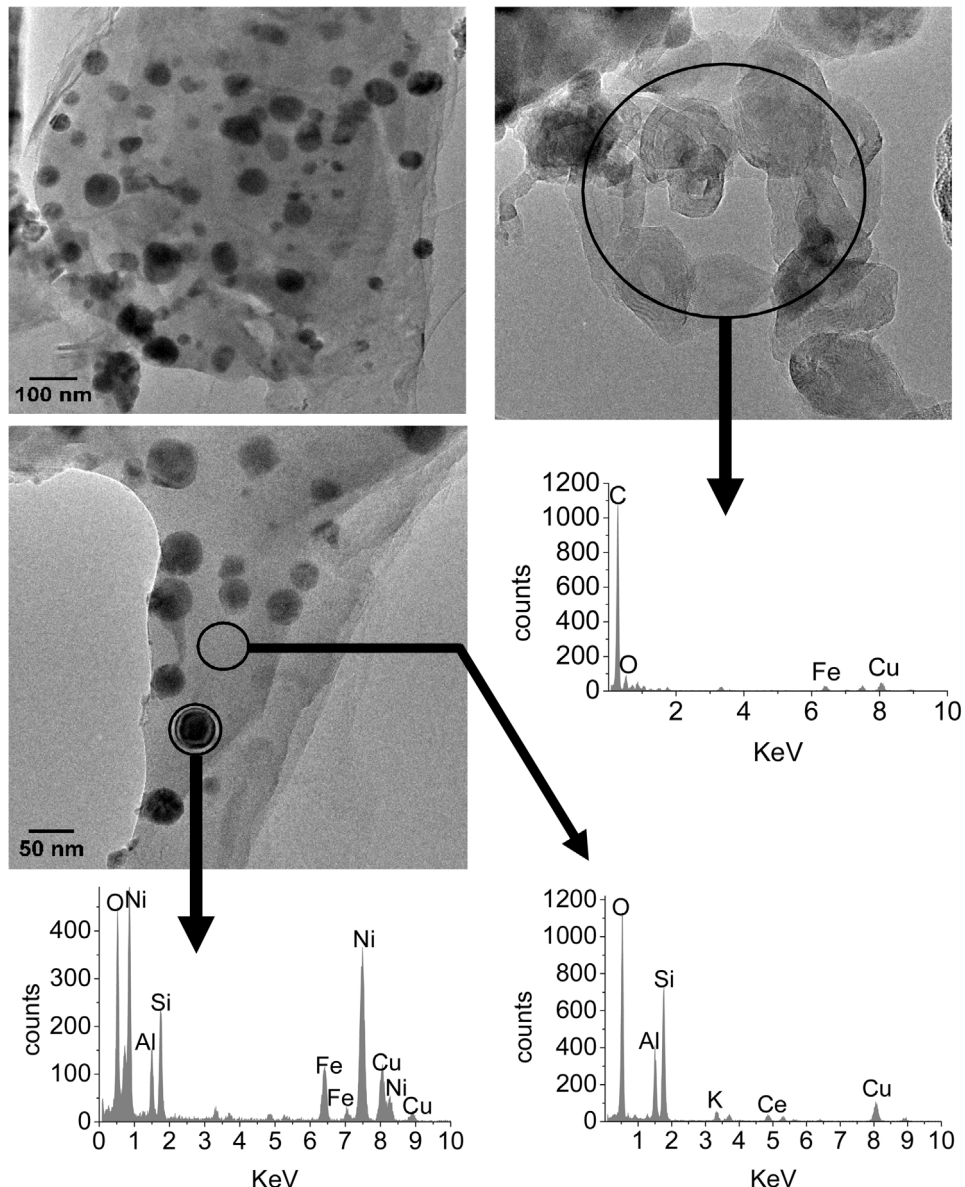


Fig. 12. TEM and EDX analysis on 10Ni15Ce after 24 h of reaction.

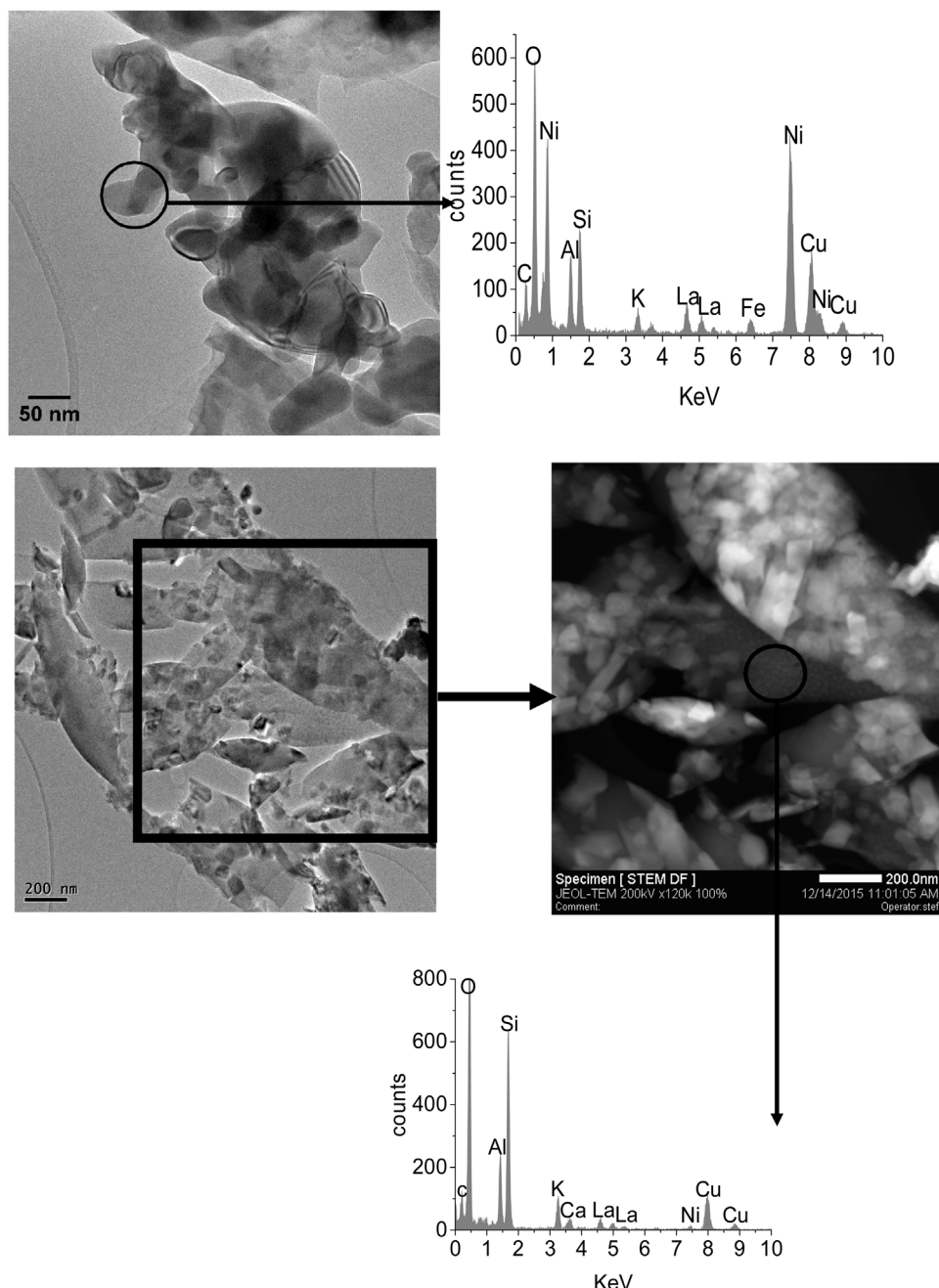


Fig. 13. TEM and EDX analysis on 10Ni15La after 24 h of reaction.

Contrary to Ce the oxidation state of lanthanum is not modified during reaction (La^{3+}). The oxygen introduced into the gaseous flow can oxidize both the deposited carbon and nickel leading to NiO formation [36]. Nickel oxide is then reduced by methane restoring the metallic nickel site. Furthermore, the basic surface sites, revealed by CO_2 -TPD, can also play a significant role as already reported by different authors, for example through cooperative interaction between nickel sites and basic oxide leading to enhanced CO_2 adsorption and methane activation [20,37].

Moreover, the nickel particle size, after reaction, appear significantly lower in the case of La containing catalyst as compared to Ce, which can explain the improved stability of the 10Ni15La catalyst.

3.3.2. Surface characterization by XPS analysis

3.3.2.1. 10Ni15Ce samples. *Ex situ* XPS analysis were performed on the calcined and used samples after dry reforming reaction. *In situ*

reduction was carried out at 600°C in 10 vol.% H_2 in He. The survey spectra recorded on calcined La and Ce-doped natural illite clay in Fig. S1 (Supplementary Materials) characterize various elements in agreement with the elemental composition given in Table S1 (Supplementary Materials).

Particular attention was paid to the $\text{Ni} 2\text{p}$, $\text{Ce} 3\text{d}$, $\text{O} 1\text{s}$ and $\text{C} 1\text{s}$ photopeaks reported in Fig. 14(A)–(D) for 10Ni15Ce. The normalized $\text{Ni} 2\text{p}$ spectrum (Fig. 14(A)-a) recorded on the calcined sample exhibits complex features associated to the multiplet splitting of the $\text{Ni} 2\text{p}_{3/2}$ transition with two components at 853.7 and 855.5 eV and the shake up satellite structure at 861 eV characterizing Ni^{2+} likely stabilized as NiO as reported elsewhere [38,39]. *In situ* H_2 -reduction leads to a strong attenuation of the $\text{Ni} 2\text{p}$ photopeak with the disappearance of the satellite structure and a significant shift to lower binding energy values from 853.7 eV to 852.5 eV characterizing the stabilization of metallic Ni^{00} species. Interestingly, the

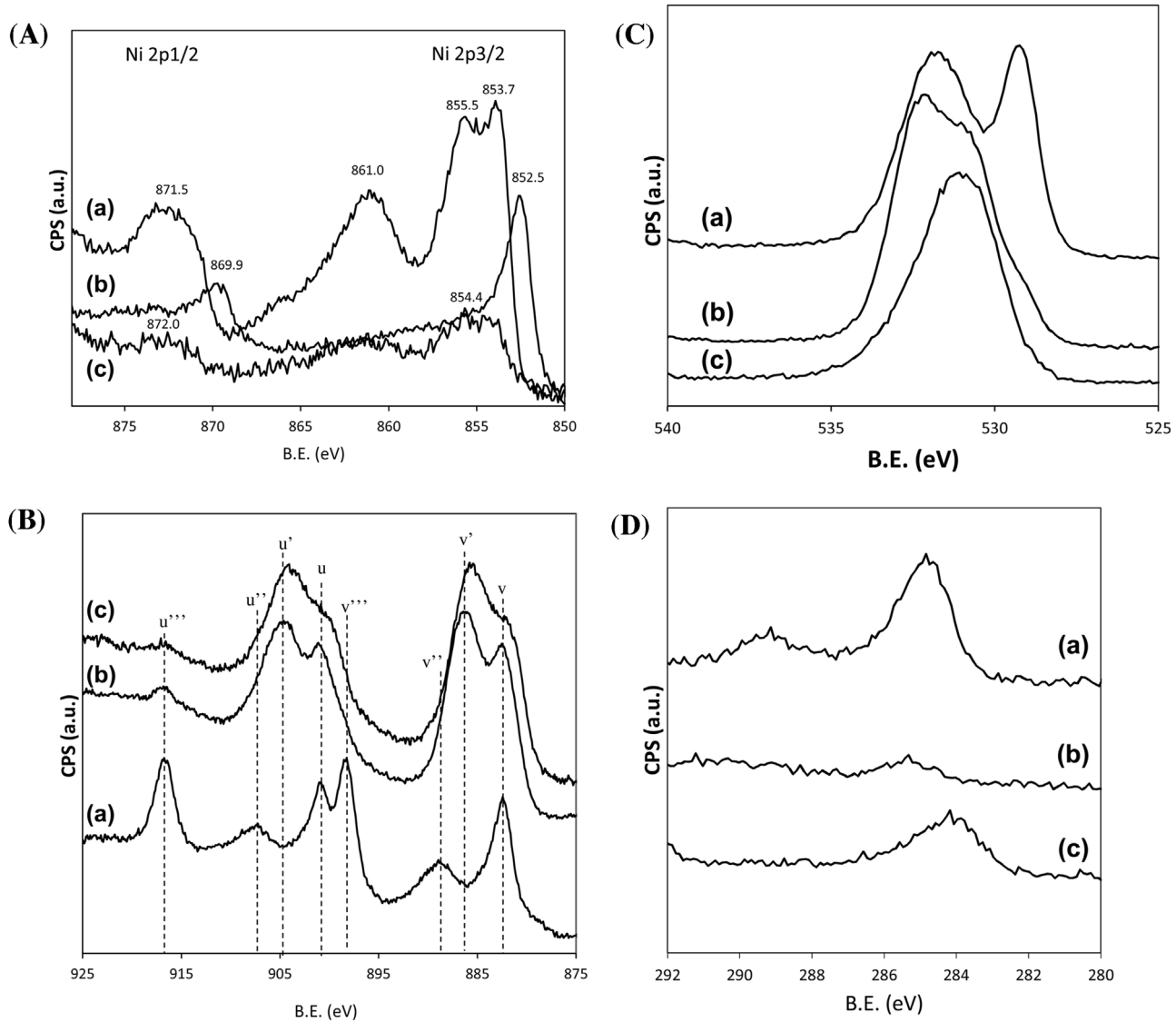


Fig. 14. (A) Normalized Ni 2p photopeak recorded on calcined 10Ni15Ce sample (a), after *in situ* reduction in 10 vol.% H₂ in He (b) after reaction (c). (B) Normalized Ce 3d photopeak recorded on calcined 10Ni15Ce sample (a), after *in situ* reduction in 10 vol.% H₂ in He (b) after reaction (c). (C) O1s photopeak recorded on calcined 10Ni15Ce sample (a), after *in situ* reduction in 10 vol.% H₂ in He (b) after reaction (c). (D) C1s photopeak recorded on calcined 10Ni15Ce sample (a), after *in situ* reduction in 10 vol.% H₂ in He (b) after reaction (c).

metallic character of nickel is not preserved on the used catalyst with B.E. values at 854.4 eV. As earlier explained such an observation could be related to particle size effects and/or the formation of intermetallic compounds [38,39]. Normalized Ce 3d spectra are collected in Fig. 14(B) composed of two spin orbit components, Ce3d_{5/2} and Ce3d_{3/2} [40], previously decomposed in five contributions, the lowest ones corresponding to u⁰⁰ and v⁰⁰ being not reported in Fig. 14(B) due to significant overlapping especially for u⁰⁰ masked by the v'' and u contributions. As seen the spectra recorded on the calcined sample is dominated by the u(v), u''(v'') and u'''(v''') contributions which reflect the presence of Ce⁴⁺. On the other hand, the contributions u(v) and u'(v') become predominant after *in situ* reduction reflecting a preferential stabilization of Ce³⁺. Interestingly the contributions u(v) and u'(v') intensify on the used catalyst after reaction evidencing a more reduced surface state compared to the pre-reduced sample in hydrogen which can be consistent with the formation of Ce_{4.67}O₁₃Si₃ as previously observed from XRD data. The examination of the O1s (Fig. 14(C)) reveals two contributions near 529 eV and 531 eV on the calcined sample previously ascribed to surface oxygen lattices and chemisorbed oxygen

species respectively [41]. Significant changes occur on the spectra recorded after *in situ* reduction and on the used sample after reaction with significant shifts of the signals to higher B.E. values and a strong attenuation on the low B.E. contribution related to surface oxygen lattices O²⁻. The shift observed on the B.E. likely reflects changes in chemical environment with different geometry and coordination for those oxygen species. The disappearance of the 529 eV contribution on the used sample underlines an extensive reduction under reaction conditions in rather good agreement with changes observed on the spectral features for the Ce 3d photopeak. The two components on the C1s photopeak in Fig. 14(D) appear at 289.2 eV at carbon species at 284.8 eV previously ascribed to C=O bond due to the presence of carbonates and C—C and C—H bonds respectively [42]. As observed, *in situ* reduction cleans the surface with a quasi-disappearance of the carbon fingerprint. However, carbon reformation takes place during the reaction as exemplified in Fig. 14(D)-c which is currently explained by coke formation during the dry reforming reaction.

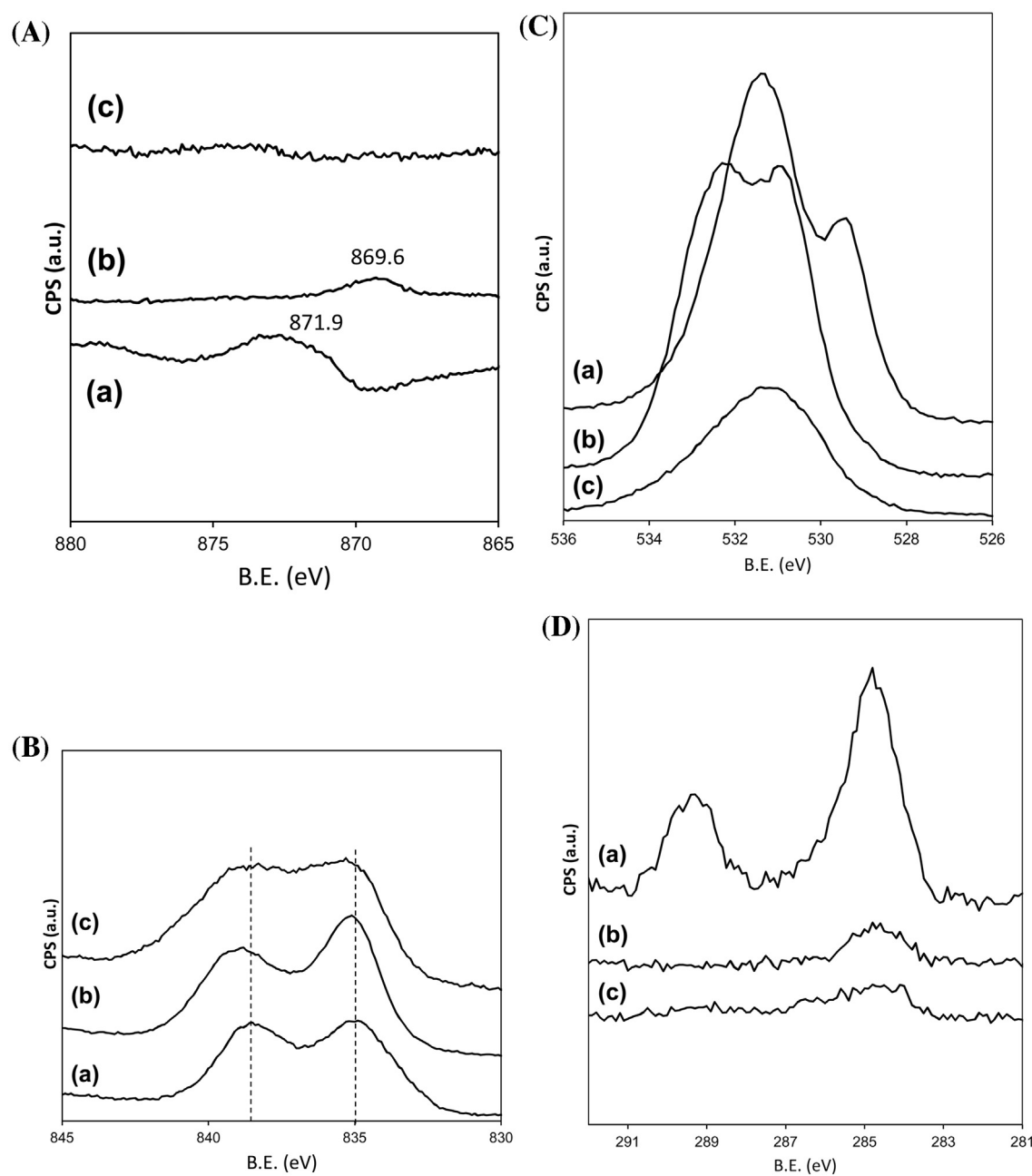


Fig. 15. (A) Normalized Ni 2p1/2 photopeak recorded on calcined 10Ni15La sample (a), after *in situ* reduction in 10 vol.% H₂ in He (b) after reaction (c). (B) Normalized La 3d5/2 photopeak recorded on calcined 10Ni15La sample (a), after *in situ* reduction in 10 vol.% H₂ in He (b) after reaction (c). (C) O1s photopeak recorded on calcined 10Ni15La sample (a), after *in situ* reduction in 10 vol.% H₂ in He (b) after reaction (c). (D) C1s photopeak recorded on calcined 10Ni15La sample (a), after *in situ* reduction in 10 vol.% H₂ in He (b) after reaction (c).

Table 4

XPS spectral features of freshly-prepared, pre-reduced and 10Ni15Ce and 10Ni15La samples after 24 h of reaction at 800 °C XPS spectral features of freshly-prepared, pre-reduced and 10Ni15Ce and 10Ni15La samples after reaction.

Catalyst	Thermal		Binding Energy (eV)			Surface composition		
	Treatment	Ni 2p3/2	Ni 2p1/2	La 3d5/2	Ce 3d5/2	Ni/La	Ni/Ce	C _{surf} (%)
10Ni15Ce	Fresh	853.7	871.5		882.3		1.72	13.8
	Prereduced	852.5	869.6		882.3		0.32	1.8
	Used	854.4	872.0		882.5		0.22	8.9
10Ni15La	Fresh	–	871.9	834.7		2.5		16.6
	Prereduced	–	869.6	835.0		0.24		2.4
	Used	–	n.m.	835.0		n.m.		8.4

3.3.2.2. 10Ni15La samples. Similar spectral features are observable on the Ni 2p core level (see Fig. 15(A)) compared to 10Ni15Ce except after reaction because no nickel is significantly detected. Due to overlapping with the La_{3d}_{3/2} photopeak, the Ni2p_{1/2} core level was preferentially examined with binding energy at 871.9 eV highlighting a predominant formation of Ni²⁺ as NiO on the calcined sample (Fig. 15(A)-a) then extensively reduced to Ni metal during the *in situ* thermal treatment in agreement with a significant shift to 869.6 eV. Regarding the La 3d photopeak (see Fig. 15(B)), earlier investigations revealed complex spectral features [43]. The binding energy values near 835 eV (see Table 4) characterized the presence of La³⁺. Subsequent differentiation between La³⁺ species in lanthanum oxide La₂O₃ or lanthanum hydroxide La(OH)₃ is not easy but can be discussed simultaneously with the examination of the O1s photopeaks reported in Fig. 15(C) which give rise at least two components. As reported elsewhere, Sunding et al. [43] identified on the O1s spectrum two strong contributions at 530.5 and 532.4 eV for La₂O₃ while they would appear at 531.4 and 529.2 eV for La(OH)₃. These assignments seem in rather good agreement with spectra in Fig. 15(C) also characterized by two maxima at 529.4 and 532.5 which seem more in agreement with the formation of La(OH)₃ on the calcined sample whereas the contributions appearing at 530.8 and 532.5 eV would reflect a preferential stabilization of La₂O₃ on the reduced sample. After reaction, a broad and poorly resolved signal appears on the La 3d photopeak likely composed of different components. Such disturbances could be associated with the formation of the mixed La_{9.31}O₂₆Si_{6.24} oxide but in all cases La(+III) species are stabilized. Similarly to 10Ni15Ce the C1s photopeak in Fig. 15(D) is composed of two contributions at 284.8 and 289.4 eV characterizing the presence of carbon and carbonates respectively consistently with the usual formation of lanthanum oxycarbonates.

3.3.2.3. Semi-quantitative analysis. Subsequent quantifications are summarized in Table 4 through the estimation of the atomic Ni/La and Ni/Ce and the relative composition of carbon. As above-mentioned the comparison of estimates of the relative concentration of surface carbon species does not highlight different affinity towards carbon deposition. It is worthwhile to note that *in situ* reduction has a detrimental effect lowering the surface Ni concentration such being more accentuated on used samples after reaction in connection with a greater extent of reduction. The comparison of Ni/La and Ni/Ce is not easy after reaction with nickel undetected on 10Ni15La compared to 10Ni15Ce.

3.4. Bulk vs. surface properties: consequences in the catalytic performances

Obviously, the catalytic behavior of 10Ni15Ce and 10Ni15La strongly differs in terms of stability: 10Ni15La exhibits a good durability in terms of conversion and selectivity, with preservation of the H₂/CO ratio, whereas, 10Ni15Ce gradually loses its activity in methane and CO₂ conversion with a concomitant decrease of the H₂/CO ratio. H₂/CO~1 is recognized as an important criterion for high syngas yields, consequently, a lowering could represent a significant drawback from a practical viewpoint. As earlier found [24], oxygen addition to the gas mixture induces a beneficial effect on methane conversion with H₂/CO~1 reasonably explained by the involvement of partial oxidation of methane minimizing the impact of the RWGS reaction on the H₂/CO ratio. This is particularly true on 10Ni15La, with methane conversion of 80% and H₂/CO=0.85 kept constant during the whole duration of the catalytic experiment. In these operating conditions, an important issue provided by this study is related to the minimization of coke formation representing the major deactivation phenomenon. However, previous investigations also shown that particle sintering [44] and oxida-

tion of metallic sites at the usual reaction temperature [45] can induce deactivation phenomena. Previous mechanistic studies on dry reforming of methane suggested the importance of metallic particles for the methane decomposition and strong CO₂ adsorption on basic materials as supports, such as La₂O₃ and CeO₂, with subsequent surface reactions between oxy-carbonate species and carbodic species at the metal-support interface [46,47]. CO₂ dissociation has been also suggested as key step [48] to promote CO production which led to the conclusion that OSC properties, non-stoichiometry, stabilization of anionic vacancies, strength of CO₂ adsorption, can govern the catalytic properties and also the extent of metal dispersion [49]. This seems consistent with our observation from TEM in Figs. 7 with smaller Ni particles on La and Ce-promoted samples. On the other hand, sintering of nickel particles is noticeable on used 10Ni15La and 10Ni15Ce catalysts which can be partly explained by a significant loss of the specific surface areas. However, it is worthwhile to note that 10Ni15La seems more resistant to thermal sintering with the preservation of lower Ni particles compared to 10Ni15Ce. A prominent information is also related to alloying effects with the formation of less active intermetallic Ni₃Fe particles on 10Ni15Ce whereas reoxidation of Ni⁰⁰ particles during the reaction into larger NiO aggregates would occur on 10Ni15La as evidenced from XRD analysis. In this latter case the appearance of bulk oxidic Ni species cannot be simply related to the catalytic properties because 10Ni15La preserves its catalytic performances which could suggest that the nickel phase itself cannot completely explain changes in catalytic properties but also concern the structural features of the promoted-illite support and more precisely the metal-support interface. As aforementioned, CeO₂ should play a key role through the modulation of its oxidation state responsible of its redox and OSC properties. As seen, peculiar interactions between CeO₂ and illite could be detrimental to its catalytic properties. As explained, the extensive formation of Ce_{4.67}O₁₃Si₃ on 10Ni15Ce could moderate the valence changes between Ce⁴⁺ and Ce³⁺ and then weaken the redox behavior.

XPS data complements bulk observations on a depth of 5–10 nm which reflects more significantly the electronic properties and composition of the outermost layer directly in contact with the reaction mixture. An important outcome comes from the examination of the Ni 2p core level on 10Ni15Ce after reaction with B.E. values characteristic of Ni²⁺ opposite to the observation of bulk metallic Ni species from XRD analysis. Such an apparent discrepancy could be likely explained by the limit of detection of XRD for analyzing highly dispersed species in low concentration. As a matter of fact, preferential interaction between metallic Ni particles and OSC materials such ceria could prevent reoxidation. In case of stabilization of Ce³⁺ in Ce_{4.67}O₁₃Si₃ further blocking valence change into Ce⁴⁺, then well-dispersed Ni⁰⁰ in the outermost layer would be no longer protected to reoxidation. Such an assumption seems in relative good agreement with spectral features observed on the O 1s and Ce 3d spectra revealing a more extensive reduction into Ce³⁺ compared to the pre-reductive treatment in hydrogen with a disappearance of the component ascribed to surface oxygen lattices on the O1s spectra. Now regarding 10Ni15La, it seems not easy to properly explain the relatively stable performances while significant bulk and surface reconstructions take place as aforementioned. Contrarily to the predominant formation Ce_{4.67}O₁₃Si₃ on 10Ni15Ce, the britholite phase La_{9.31}O₂₆Si_{6.24} would form in much lower extent and XRD analysis clearly indicates the presence of La₂O₃. Based on this observation, further interaction between La₂O₃ and Ni particle could protect them from thermal sintering as reported elsewhere [19]. On the other hand the loss, of such interactions could speed up Ni⁰⁰ reoxidation leading to bulk detectable NiO clusters.

4. Conclusions

The illite obtained from natural clay, was successfully used as catalyst support of nickel for the autothermal dry reforming of methane. The presence of lanthanum markedly improves the catalytic stability during 24 hours h of reaction at 800 °C at a space velocity of 60,000 mL g⁻¹ h⁻¹. The methane and carbon dioxide conversion are maintained close to 80 and 63% respectively during time on stream while in the presence of cerium, CH₄ conversion drops from 85 to 50% and CO₂ conversion from 62% to 40%. The Ce-based catalyst is strongly modified during reaction at 800 °C under the reaction mixture: the formation of an alloy between nickel and iron (from the illite support) is observed, this FeNi₃ alloy being less active than Ni° with respect to methane conversion. Of interest, the formation of britholite phase as result from the migration of lanthanum into the bulk. This particular phase can limit the formation of the alloy, yielding to more nickel available for the activation of methane and carbon dioxide which helps to maintain higher catalytic performances. The surface characterization carried out with XPS analysis confirmed that surface reconstruction occurs during reaction and considerably enhances the nickel species predisposed for catalytic activity and stability towards methane dry reforming.

Acknowledgements

The authors greatly acknowledge the financial support from Volubilis (MA/13/288- Campus France N°29091UK) and the Erasmus Mundus – Al Idrisi II program. Chevreul Institute (FR 2638), Ministère de l'Enseignement Supérieur et de la Recherche, Région Nord - Pas de Calais and FEDER are acknowledged for supporting and funding partially this work.

Appendix A. Supplementary data

Supplementary data associated with this article can be found, in the online version, at <http://dx.doi.org/10.1016/j.apcatb.2016.12.050>.

References

- [1] J.R. Rostrup-Nielsen, J. Sehested, J.K. Norskov, *Adv. Catal.* 47 (2002) 65–139.
- [2] S.C. Tsang, J.B. Claridge, M.L.H. Green, *Catal. Today* 23 (1995) 3–15.
- [3] J.T. Richardson, S.A. Paripatyadar, *Appl. Catal.* 61 (1990) 293–309.
- [4] A.T. Ashcroft, A.K. Cheetman, M.L.H. Green, P.D.F. Vernon, *Nature* 352 (1991) 225–226.
- [5] F. Solymosi, G. Kutsan, A. Erdöhelyi, *Catal. Lett.* 11 (1991) 149–156.
- [6] O. Yamazaki, T. Nozaki, K. Omata, K. Fujimoto, *Chem. Lett.* (1992) 1953–1954.
- [7] Y.H. Hu, E. Ruckenstein, *Catal. Lett.* 36 (1996) 145–149.
- [8] U. Slagtern, R. Olsbye, I.M. Blom, H. Dahl, F. Jellvag, *Appl. Catal. A* 145 (1996) 375–388.
- [9] S. Wang, G.Q. Lu, *Appl. Catal. B: Environ.* 16 (1998) 269–277.
- [10] J. Chen, R. Wang, J. Zhang, F. He, S. Han, *J. Mol. Catal. A* 235 (2005) 302–310.
- [11] R. Craciun, B. Shereck, R.J. Gorte, *Catal. Lett.* 51 (1998) 149–153.
- [12] H.C. Yao, Y.F.Y. Yao, *J. Catal.* 86 (1984) 254–265.
- [13] X. Verykios, *Int. J. Hydrogen Energy* 28 (2003) 1045–1063.
- [14] S. Wang, H.Y. Zhu, G.Q. Lu, *J. Colloid Interface Sci.* 204 (1998) 128–134.
- [15] K.S. Hwang, H.Y. Zhu, G.Q. Lu, *Catal. Today* 60 (2001) 183–190.
- [16] R. Debek, M. Radlik, M. Motak, M.E. Galvez, W. Turek, P. Da Costa, T. Grzybek, *Catal. Today* 257 (2015) 59–65.
- [17] C.E. Daza, J. Gallego, F. Mondragon, S. Moreno, R. Molina, *Fuel* 89 (2010) 592–603.
- [18] A. Serrano-Lotina, L. Rodriguez, G. Munoz, A.J. Martin, M.A. Folgado, L. Daza, *Catal. Commun.* 12 (2011) 961–967.
- [19] X. Yu, N. Wang, W. Chu, M. Liu, *Chem. Eng. J.* 209 (2012) 623–632.
- [20] H. Liu, D. Wierzbicki, R. Debek, M. Motak, T. Grzybek, P. Da Costa, M.E. Gálvez, *Fuel* 182 (2016) 8–16.
- [21] C.E. Daza, A. Kiennemann, S. Moreno, R. Molina, *Appl. Catal. A: gen.* 364 (2009) 65–74.
- [22] T. Kimura, H. Kawashima, I. Saito, *Int. J. Coal Geol.* 26 (1994) 215–231.
- [23] A. Cremers, A. Elsen, P. Depreter, A. Maes, *Nature* 335 (1988) 247–249.
- [24] M. Akri, T. Chafik, P. Granger, P. Ayraut, C. Batiot-Dupeyrat, *Fuel* 178 (2016) 139–147.
- [25] A.M. O'Connor, J.R.H. Ross, *Catal. Today* 46 (1998) 203–210.
- [26] N. Fairley, <http://www.casaxps.com>, ©Casa Software Ltd., 2005 (version 2.3.16).
- [27] H. Gailhanou, P. Blanc, J. Rogez, G. Mikaelian, H. Kawaji, J. Olives, M. Amouric, R. Denoyel, S. Bourrelly, V. Montouillout, P. Vieillard, C.I. Fialips, N. Michau, E.C. Gaucher, *Geochim. Cosmochim. Acta* 89 (2012) 279–301.
- [28] H.M. Baioumy, M.H.M. Gharaie, *Appl. Clay Sci.* 42 (2008) 318–325.
- [29] H. Provendier, C. Petit, C. Estournes, A. Kiennemann, *Stud. Surf. Sci. Catal.* 119 (1998) 741–746.
- [30] B. Li, X. Xu, S. Zhang, *Int. J. Hydrogen Energy* 38 (2013) 890–900.
- [31] R. Martínez, R. Romero, C. Guimon, R. Bilbao, *Appl. Catal. A Gen.* 274 (2004) 139–149.
- [32] N.A.S. Amin, T.C. Yaw, *Int. J. Hydrogen Energy* 32 (2007) 1789–1798.
- [33] V.V. Galvita, H. Poelman, C. Detavernier, G.B. Marin, *Appl. Catal. B* 164 (2015) 184–191.
- [34] K.Y. Koo, S.H. Lee, U.H. Jung, H.S. Roh, W.L. Yoon, *Fuel Process. Technol.* 119 (2014) 151–157.
- [35] S.M. Lima, J.M. Assaf, M.A. Pena, J.L.G. Fierro, *Appl. Catal. A: Gen.* 311 (2006) 94–104.
- [36] L. Pino, A. Vita, M. Lagana, V. Recupero, *Appl. Catal. B: Environ.* 148–149 (2014) 91–105.
- [37] (a) Z. Zhang, X.E. Verykios, *Appl. Catal. A* 138 (1996) 109;
- [38] (b) X.E. Zhang, *Catal. Lett.* 38 (1996) 175–179.
- [39] E. Heracleous, A.F. Lee, K. Wilson, A.A. Lemonidou, *J. Catal.* 231 (2005) 159–171.
- [40] J.P. Espinosa, A.R. Gonzalezelipe, A. Fernandez, G. Munuera, *Surf. Interface Anal.* 19 (1992) 508–512.
- [41] F. Le Normand, J. El Fallah, L. Hilaire, P. Légaré, A. Kotani, J.C. Parlebas, *Solid State Commun.* 71 (11) (1989) 885–889.
- [42] S. Ponce, M.A. Peña, J.L.G. Fierro, *Appl. Catal. B* 24 (2000) 193–205.
- [43] H. Estrade-Szwarckopf, *Carbon* 42 (2004) 1713–1721.
- [44] M.F. Sunding, K. Hadidi, S. Dilas, O.M. Løvvik, T.E. Norby, A.E. Gunnæs, J. Electron Spectrosc. Relat. Phenom. 184 (2011) 399–409.
- [45] Z.L. Zhang, V.A. Tsipouriari, A.M. Efstathiou, X.E. Verykios, *J. Catal.* 158 (1996) 51–63.
- [46] H.Y. Ruckenstein, E. Wang, *J. Catal.* 205 (2002) 289–293.
- [47] V.A. Tsipouriari, X.E. Verykios, *Catal. Today* 64 (1–2) (2001) 83–90.
- [48] J.F. Munera, S. Irusta, L.M. Cornaglia, E.A. Lombardo, D. Vargas Cesar, M. Schmal, *J. Catal.* 245 (1) (2007) 25–34.
- [49] M.S. Aw, I.G. Osojnik, P. Djinovic, A. Pintar, *Int. J. Hydrogen Energy* 39 (2014) 12636–12647.
- [50] L. Pino, A. Vita, M. Lagan, V. Recupero, *Appl. Catal. B* 148–149 (2014) 91–105.